High efficiency photonic crystal based wavelength demultiplexer

Meron Y. Tekeste and Jan M. Yarrison-Rice

Physics Department, Miami University, Oxford, OH 45056
Miami University Center for Nanotechnology, Oxford, OH 45056
tekestmy@muohio.edu, yarrisjm@muohio.edu

Abstract: A highly efficient design of a two-channel wavelength demultiplexer in the visible region is presented with finite-difference time-domain simulations. The design process is described in detail with particular attention to the challenges inherent in fabrication of an actual device. A 2D triangular lattice photonic crystal with 75nm air pores in a silicon nitride planar waveguide provides the confinement for visible light. The device losses due to fabrication errors such as stitching misalignment of write fields during e-beam lithography and variation in air pore diameters from etching are modeled using realistic parameters from initial fabrication runs. These simulation results will be used to guide our next generation design of high efficiency photonic crystal based demultiplexing devices.

OCIS codes: (999.9999) Photonic bandgap structures; (060.1810) Couplers, switches, and multiplexers; (220.3740) Optical design and fabrication, lithography

References and links

1. S. G. Johnson, J. D. Joannopoulos, "Designing synthetic optical media: Photonic Crystals," Acta. Mater. **51**, 5823-5835 (2003).
2. T. A. Birks, J. C. Knight, and P. St. J. Russell, "Endlessly single-mode photonic crystal fiber," Opt. Lett. **22**, 961–963 (1997).
3. T. D. Happ, A. Markard, M. Kamp, A. Forchel, S. Anand, J.-L. Gentner, and N. Bouadma, "Nano-fabrication of two-dimensional photonic crystal mirrors for 1.5 µm short cavity lasers," J. Vac. Sci. Technol. B **19**, 2775–2778 (2001).
4. M. Loncar, T. Yoshie, A. Scherer, P. Gogna, and Y. Qiu, "Low-threshold photonic crystal laser," Appl. Phys. Lett. **81**, 2680–2682 (2002).
5. E. Centeno, B. Guizal, and D. Felbacq, "Multiplexing & demultiplexing with photonic crystal," J. Opt. A: Pure Appl. Opt. **1**, L10-L13 (1999)
6. C. Jin, S. Fan, S. Han, and D. Zhang, "Reflectionless multichannel wavelength demultiplexer in a transmission resonator configuration," IEEE J. Quantum Electron. **39**, 160-165 (2003).
7. S. Kim, I. Park, H. Lim, and C. -S. Kee, "Highly efficient photonic crystal-based multichannel drop filters of three-port system with reflection feedback," Opt. Express **12**, 5518-5525 (2004).
8. A. Sharkawy, S. Shi and D. W. Prather, "Multichannel wavelength division multiplexing with photonic crystals," Appl. Opt. **40**, 2247-2252 (2001).
9. M. Koshiba, "Wavelength division multiplexing and demultiplexing with photonic crystal waveguide couplers," J. Lightwave Technol., **19**, 1970-1975, (2001).
10. D. Pustai, A. Sharkawy, S. Shouyuan and D. W. Prather, "Tunable photonic crystal microcavities," Appl. Opt. **41**, 5574-5579 (2002).
11. J. Zimmermann, M. Kamp, A. Forchel, and R. Marz, "Photonic crystal waveguide directional couplers as wavelength selective optical filters," Opt. Commun. **230,** 387–392 (2004).
12. F. S. Chien, Y. Hsu, W. Hsieh, and S. Cheng, "Dual wavelength demultiplexing by coupling and decoupling of photonic crystal waveguides," Opt. Express **12**, 1119-1125 (2004).
13. B. Momeni, J. Huang, M. Soltani, M. Askari, S. Mohammadi, M. Rakhshandehroo, and A. Adibi, "Compact wavelength demultiplexing using focusing negative index photonic crystal superprisms," Opt. Express **14**, 2413-2422 (2006).
14. N. J. Florous, K. Saitoh, and M. Koshiba, "Three-color photonic crystal demultiplexer based on ultralow-refractive-index metamaterial technology," Opt. Lett. **30**, 2736-2738 (2005) http://www.opticsinfobase.org/abstract.cfm?URI=ol-30-20-2736

#71934 - $15.00 USD Received 13 June 2006; revised 7 August 2006; accepted 8 August 2006

15. T. Niemi, L. H. Frandsen, K. K. Hede, A. Harpoth, P. I. Borel, and M. T. Kristensen, " Wavelength-division demultiplexing using photonic crystal waveguides," IEEE Photon. Technol. Lett. **18**, 226-228 (2006).
16. FDTD computation by EMPLab software running on EMPhotonics Computer.
17. S. Fan and J. D. Joannopoulos, "Analysis of Guided Resonances in Photonic crystal slabs," Phys. Rev B **65**, 235112 (2001).
18. K. Kawano and T. Kitoh, *Introduction to Optical Waveguide Analysis*, (John Wiley & Sons, 2001), Chap. 2.
19. J. D. Joannopoulos, R. D. Meade, J. N. Winn, *Photonic Crystals: Molding the Flow of Light* (Princeton, NJ. Princeton University Press, 1995), Chap. 5.
20. M. Koshiba, M. Tsuji, and Y. Sasaki, "High-performance absorbing boundary conditions for photonic crystal waveguide simulations," IEEE Microwave Wirel. Compon. Lett. **11**, 152-154 (2001).
21. A. Mekis, S. Fan, and J. D. Joannopoulos, "Bound states in photonic crystal waveguides and waveguide bends," Phys. Rev. B **58**, 4809 (1998).
22. M. Tekeste, and J. Yarrison-Rice, "Modeling and fabrication results of a photonic crystal based wavelength demultiplexers," in *Proceedings of IEEE Conference on Nanotechnology 2006*, (To be published).
23. R. Wüest, P. Strasser, M. Jungo, F. Robin, D. Erni, and H. Jäckel "An efficient proximity- effect correction method for electron-beam patterning of photonic-crystal devices," Microelectron. Eng. **67-68**, 182-188 (2003).

1. Introduction

A photonic crystal is an artificial material that gives us the ability to control the propagation of light by the addition of particular defects within the regular photonic lattice [1]. A photonic crystal's ability to guide light efficiently and to confine a single wavelength within the crystal makes them a promising addition to the currently available electron-based semiconductor devices. A number of different photonic band gap (PBG) optoelectronic devices have been implemented since 1987 including photonic crystal based fiber optics [2], frequency selective mirrors, filters [3], and efficient lasers [4]. Moreover, several example applications for telecommunication such as wavelength division multiplexing and wavelength division demultiplexing (WDDM) have been proposed [5-10]. In realizing the photonic crystal based WDDM, different wavelength selective filtering techniques have been used. Waveguide based filters which utilize coupling between two closely spaced waveguides [11, 12], filters that couple two waveguides using a cavity [5-10], and negative refractive index super-prism based filters [13] are some of the examples which have recently been used to achieve PC based wavelength demultiplexing. In addition, demultiplexing has also been achieved by varying the PBG waveguide edge pore diameters [14, 15].

Our research is aimed at studying the demultiplexing capabilities of photonic crystals in the visible region with the ultimate goal of fabricating such a device structure. The device is fabricated in a planar waveguide, which consists of silicon nitride (Si_3N_4) on silicon dioxide (SiO_2). A triangular photonic lattice will confine light that propagates in the 2D-plane and confinement in the direction perpendicular to the plane occurs via the traditional high index method. Our WDDM is modeled using a photonic crystal slab [17] that consists of an input waveguide, output channels and cavities that couple a specific wavelength into the exit channels [7,8,10]. In addition, a PBG mirror is introduced into the input waveguide to enhance the output coupling [7], and the waveguide and output channels are tailored to support single mode propagating of only the particular wavelength of interest.

Using the Finite-Difference Time-Domain (FDTD) computational method [21], we model and analyze device structure characteristics until the parameters for a high efficiency wavelength demultiplexer are identified. In the first section the theoretical background of electromagnetic propagation in a three layer (SiO_2-Si_3N_4-Air) thin film and in 2D photonic crystal is presented briefly. Next, the model and its simulation results for a two-channel wavelength demultiplexer are presented and the corresponding channel transmission output is reported. Because fabrication of real devices automatically implies errors, as instruments never operate perfectly and processing introduces other errors, it is important to consider how such errors affect ultimate device performance. Thus, the losses due to the stitching error (horizontal and vertical shift) and air pore diameter variability, which occur during different fabrication steps, are simulated based on initial fabrication runs. Finally we arrive at a WDDM design, which results in a controlled, highly efficient output for each of the two input wavelengths.

#71934 - $15.00 USD Received 13 June 2006; revised 7 August 2006; accepted 8 August 2006

2. High index method

We first address the vertical layers of the planar waveguide and determine the thickness for the core layer, which will allow for single mode propagation for selected argon ion laser wavelengths. Solving Maxwell's equations for allowed propagation modes, a transcendental equation (Eq. 1) results for a three-layer slab optical waveguide composed of silicon dioxide (cladding), silicon nitride (core) and air (cladding) [18].

$$k_o\sqrt{n_2^2-n_{eff}^2}\,h=-\tan^{-1}\left(\frac{\sqrt{n_2^2-n_{eff}^2}}{\sqrt{n_{eff}^2-n_1^2}}\right)-\tan^{-1}\left(\frac{\sqrt{n_2^2-n_{eff}^2}}{\sqrt{n_{eff}^2-n_3^2}}\right)+(q+1)\pi \qquad (1)$$

Here h is the silicon nitride thickness; q is an integer that represents the mode number; and n_{eff} is the effective refractive index [$n_3(n_{SiO2}) < n_{eff} < n_2(n_{Si3N4})$].

Solutions to the transcendental equation [Eq. (1)] show that among the discrete solutions to the wave equation, there are allowed non-decaying modes that propagate through the three layers without loss. These non-decaying eigenmodes depend on the thickness of the nitride layer and the refractive index of the layers. We find that single mode propagation can be achieved for a wavelength of 514.5 nm when the nitride thickness is 200nm. Upon further consideration of the wavelength dependency, we find that single modes can be achieved at 200nm thick silicon nitride for the four single mode argon laser lines at 476.5nm, 488nm, 496.5, and 514.5nm.

3. Photonic crystal

In this research, a photonic crystal with a triangular lattice is created inside the silicon nitride layer; with the addition of point and line defects, the light can be guided within the PBG

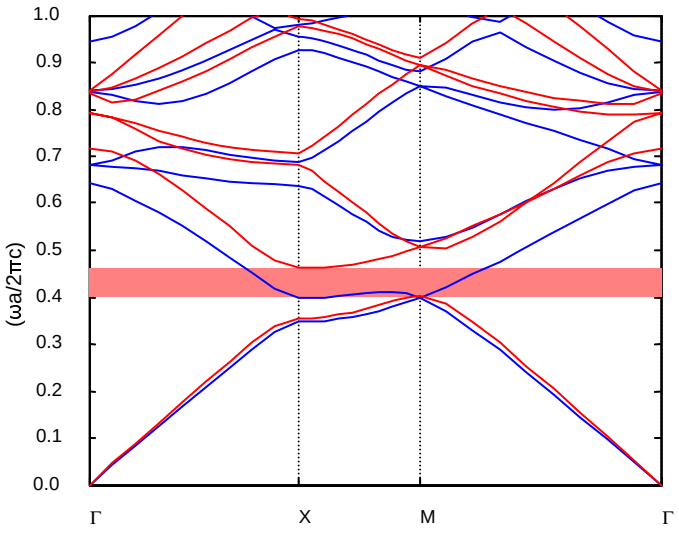

Fig. 1. A photonic band gap dispersion curve. Allowed TE modes are drawn in red, and TM modes are in blue. The PBG for TE mode ranges $0.4 < a/\lambda < 0.46$ where "a" is the lattice constant and "λ" is the free space wavelength.

lattice [19]. For a 2D triangular lattice photonic crystal with 75 nm radius air pores and 213 nm lattice constant, the dispersion curve is calculated and displayed in Fig. 1. The red lines indicate allowed transverse electric (TE) modes, while the blue lines indicate allowed transverse magnetic (TM) modes. The TE mode is defined as the mode in which light is

#71934 - $15.00 USD Received 13 June 2006; revised 7 August 2006; accepted 8 August 2006

polarized perpendicular to the air pore, or parallel to the planar waveguide-air interface. A PBG, shown in the red shaded area, is found for the TE polarization only. The photonic band gap (PBG) lies between 0.4 ($a\omega/2\pi c$) and 0.46 ($a\omega/2\pi c$) or 463 nm < λ < 532 nm. This corresponds to the wavelength region of interest - the argon ion lines between 456 nm and 514.5 nm. Such wavelengths would be totally confined in a waveguide whose sides were composed of this PBG lattice. Using these PBG and index guiding parameters, we now consider the design of a WDM device.

4. Design process and simulation

In our design and simulation steps, we use an FDTD numerical technique in which a 200nm wide absorbing boundary layer is used to reduce the back reflection from the end of the PBG lattice during computation [20]. A 10nm by 10nm grid size is used as the mesh size for the calculation. A single frequency Gaussian input source is launched inside the waveguide throughout the simulation steps that involve waveguiding. A triangular lattice consisting of a matrix of air pores is used as the basic calculational field; the number of air pore rows for each simulation is determined by the minimum number which provides repeatable results when another row is added. The electric field amplitude as a function of position within the computational area is produced as an output from the simulation.

The WDDM was designed in step-wise fashion from linear waveguide to coupling cavity to single output coupler and finally to the full demultiplexer. Each part of the device was optimized and then these parameters were incorporated in the final structure and revised as needed to achieve the best output efficiency.

4.1 Linear waveguide

Our first step was to identify the properties of a linear waveguide which had good single mode propagation and strong output transmission. By changing the waveguide width, allowed single modes for different input wavelengths can be explored [21]. We found that a linear waveguide (made by removing a single row of air pores from the lattice) with a width of 189 nm provided good confinement and high transmission for the 496.5 nm argon line, and that a waveguide width of 219 nm was optimum for 514.5 nm light. Losses of less than 1.5 % were recorded in the linear waveguide section.

4.2. High Q coupling cavity

Photonic crystals also have the ability to trap a particular wavelength of light around a point defect. This behavior is realized by changing the radius of a single air pore at the center inside the triangular photonic crystal of 9 X 9 lattice of air pores as shown in Fig. 2(a) [19]. The optimum cavity radius is determined by varying the point defect radius from zero to a maximum value for a single wavelength plane wave input source and by measuring the intensity inside the cavity. The steady state amplitude of the field propagation for the 514.5 nm high Q cavity (R = 125 nm) is recorded in Fig. 2(b), and the graphs of the relative intensity as a function of defect cavity radius for four wavelengths are seen in Fig. 2(c). The value I/Io is the intensity in the defect cavity divided by the input intensity at steady state. For the 514.5 nm spectrum line, a point defect of 125 nm radius is most effective, and for 496.5 nm line, the highest Q is seen with a defect of 135 nm radius. For the 488.0 nm and 476.5 nm two peak values from the dielectric and air band are observed [19]. For 476.5 nm spectrum line, a point defect of 165 nm and 50 nm created a high Q-cavity. The same is true for 488.0 nm with two possible cavities one with 145 nm radius and the other is when the air pore is totally removed.

#71934 - $15.00 USD Received 13 June 2006; revised 7 August 2006; accepted 8 August 2006

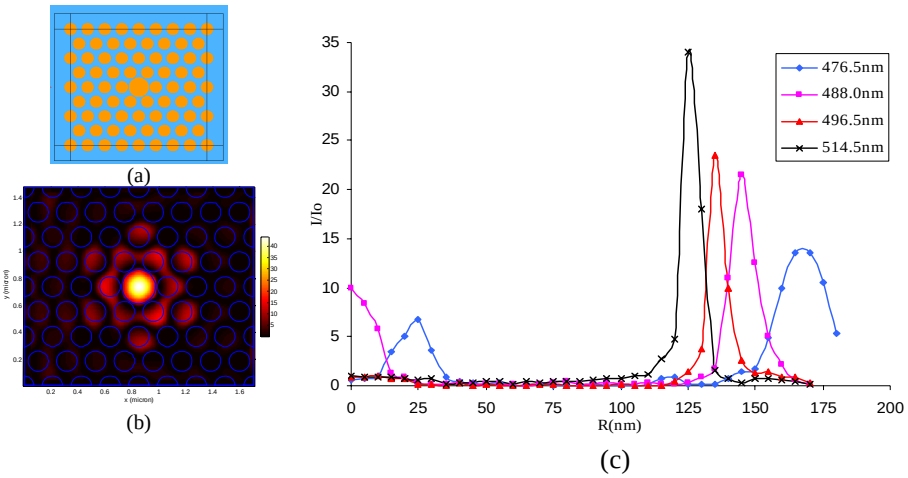

Fig. 2. (a). 9 x 9 matrix used in the simulation with a point defect at the center. (b) The simulation results in a high intensity field building up in the defect cavity when the defect size (R = 125 nm) and wavelength (λ = 514.5 nm) are well matched. (c) The normalized intensity profile for the defect cavity with different defect radii for four different wavelengths.

Thus, we have identified the highest Q defect cavity and the width of waveguide, which supports single mode propagation for each of our wavelengths. We now incorporate these features into a single wavelength output coupling structure.

4.3. Single wavelength output coupling structure

Initially a single channel wavelength output coupler is simulated [22, 23]. A 2D triangular lattice consisting of 17 X 17 matrix of air pores is used as a calculation field. A waveguide, a diagonal channel, and a cavity that couples the diagonal channel with the waveguide, are incorporated inside the crystal. The output from this structure was not as high as expected, so we added a reflector to the end of the input waveguide. When a PBG mirror (air pores) is placed at the exit end of waveguide, it enhances the output coupling through the defect cavity by approximately 20% due to the standing wave which is produced when the incident and reflected guided modes constructively interfere [7]. If the cavity is placed at a position of high interference intensity in the input waveguide, stronger coupling to the output channel is obtained. In addition, we compared the transmission efficiency of the single output coupler as a function of position of the exit channel and the defect cavity. Simulations were run when the resonant cavity was placed one lattice point to the right of the center of the output channel, when it was at the center (directly in line with the channel), and when it was one lattice point to the left of the exit channel. We found out the maximum transmission occurred when the cavity is placed one lattice point to the right below the channel (see resonant cavity placement in Fig. 3). The output transmission drops by a factor of four when the coupler is placed in either of the other positions. After these initial models were studied, we simulate the resulting single channel coupler for 514.5nm and 496.5nm wavelengths. For 514.5nm Gaussian input source, a 219nm wide waveguide and channel with 125 nm cavity radius, we obtained 86.5% transmission through the channel. A 89.2% transmission was achieved for a 496.5nm Guassian source with a 189 nm wide waveguide and channel. The transmission efficiencies are calculated by taking the ratio of the total output power to the total input power. We average along the length of the output channel to account for the standing wave which results from non-perfectly absorbing boundary conditions.

#71934 - $15.00 USD Received 13 June 2006; revised 7 August 2006; accepted 8 August 2006

4. 4. The full WDDM structure

The final design structure was produced by bringing all the results from the previous steps together. By combining two different single channel output couplers, each with their own high Q-factor resonators, a two-channel wavelength demultiplexer can be created (Fig. 3). Here the calculational field consists of a 30 x 35 matrix of air pores. To combine the two single channel output couplers into a WDDM, the 219 nm wide waveguide, which is used for the 514.5 nm output coupling has to be reduced to 189 nm for efficient 496.5 nm output coupling. Thus, we reduce the waveguide width incrementally, by 10nm per air pore column, until the waveguide width reaches 189 nm, producing a funneling effect. This waveguide reduction begins after the 514.5 nm defect cavity and coupling have occurred. As the waveguide

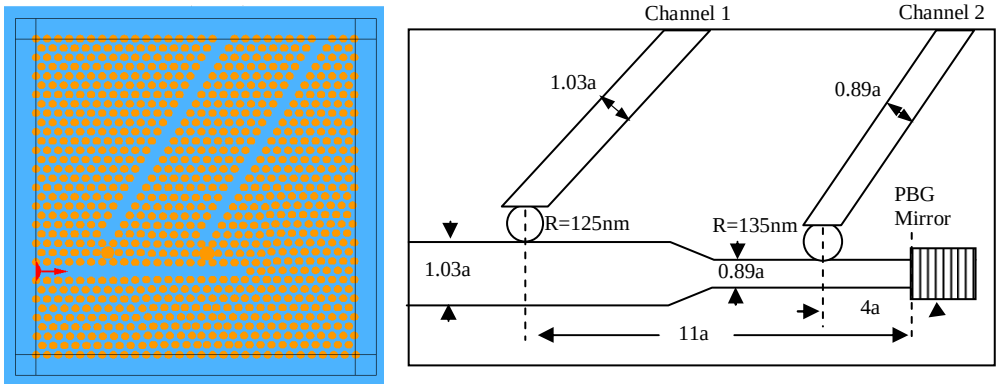

Fig. 3. Detail design of a two channel WDDM. Output Channel 1 is for 514.5 nm line and Output Channel 2 is for 496.5 nm line. The width of the waveguide is measured from edge to edge of the air pores of the photonic crystal and "a" is the lattice constant of the crystal.

becomes narrower, the 514.5 nm light is no longer able to propagate in the channel and so it is reflected. This increases the efficiency of the coupling for the 514.5 nm light and acts as a filter for the 496.5 nm coupling by not passing the 514.5 nm light into the subsequent section of the input waveguide. Again, a photonic crystal mirror is placed at the end of the waveguide. The first and the second cavities are at 11*a* and 4*a* respectively relative to the PBG mirror, so that the standing wave interference is at a high intensity at each coupling cavity. Simulations of the WDDM with and without the PBG mirror section show that the coupling to the output channels is increased from 68.2% to 86.6% for 514.5 nm and from 65.8% to 86.7% for 496.5 nm. A full frequency response of the PBG mirrored section was simulated. We find that the back reflected light within the input waveguide (near x = 1-3 microns in Fig. 4) is uniformly high (about 80%) for all frequencies until the output channel frequencies are reached. AtT the coupling frequencies, the back-reflection of the PBG mirror is utilized for coupling out through the defect cavity to the particular exit channel and the back-reflected percentage drops to ~40%. At 507 nm input, an additional loss of PBG reflection in the input waveguide is seen. This occurs because the funneling section of the input waveguide acts as a high Q cavity for 507 nm light. Back-reflection at the waveguide input drops to about 61% here.

With this design, we launch a 514.5 nm input beam, and as Fig. 4(a) displays, most of the 514.5 nm line is reflected back at the funnel and the rest is reflected back by the mirror. This back reflection in combination with the high Q-factor of the cavity increases the transmission intensity at output channel 1. A 86.6% transmission is measured along the channel 1 with only a 4.1% loss into output channel 2. For the 496.5 nm source, the results of the simulation are displayed in Fig. 4(b). Almost all the back reflection occurs due to the PBG mirror, and the funnel acts as a resonator with a low Q-factor. We achieve 86.7% transmission efficiency along output channel 2 with 9.8% loss through output channel 1.

#71934 - $15.00 USD Received 13 June 2006; revised 7 August 2006; accepted 8 August 2006

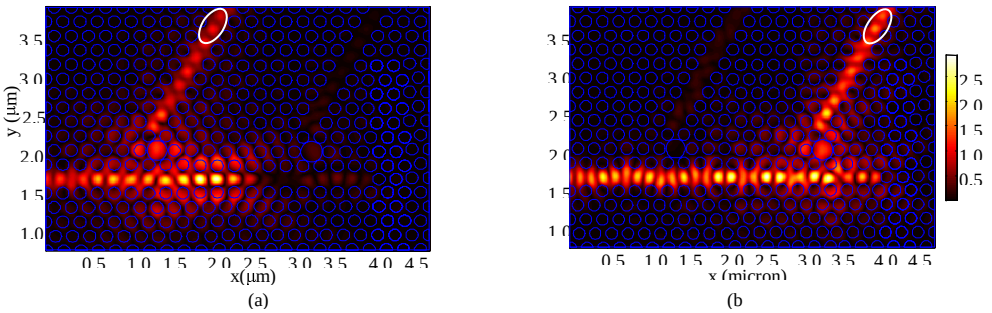

Fig. 4. (a). (1.2 MB) Movie of simulation results for a 514.5 nm spectrum line. (b). (2.1 MB) Movie of simulation results for a 496.5 nm spectrum line. In (a and b) the oval shape at the end of the channels shows the position where the average steady state was measured.

The transmission spectrum for the two output channels is shown in Fig. 5. The peak of its transmission spectrum is at 5.83 x 10^{14} Hz (514.5 nm) and 6.04 x 10^{14} Hz (496.5 nm). A figure of merit for the frequency filtering capability of this WDDM is determined as follows. The frequency of the peak transmission is divided by the full-width at half-maximum intensity to produce a "Q" for each channel. Channel 1 (514.5 nm design) has a $Q = \nu_o/\Delta\nu = 64.7$ and Channel 2 has a Q of 86.28. This provides insight into the filtering characteristics of the WDDM.

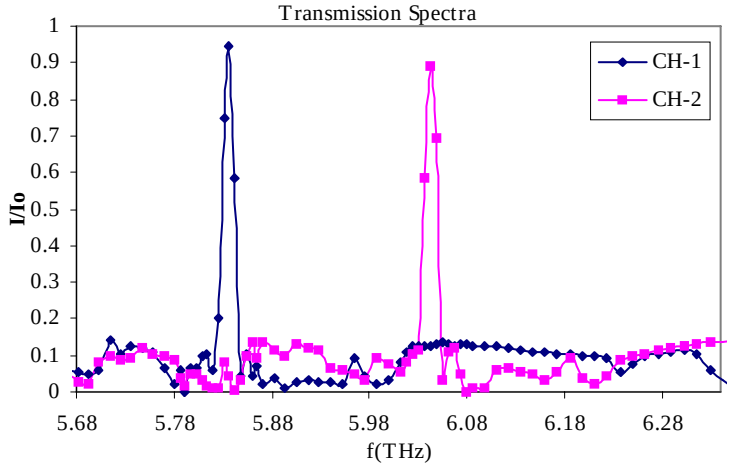

Fig. 5. Transmission spectra for each output channel as a function of input frequency.

5. Fabrication processing errors

One of the most important considerations in designing opto-electronic devices is the yield of devices when they are produced in large numbers. Thus, the errors introduced during fabrication need to be analyzed and taken into account during the design and testing phase of any prototype structures. Several sources of error are possible during fabrication including electron scattering known as the proximity effect, stitching errors, and etching anisotropies. The proximity effect is an overexposure from the e-beam writing, which occurs due to

#71934 - $15.00 USD Received 13 June 2006; revised 7 August 2006; accepted 8 August 2006

forward and back scattering of electrons, which produce additional exposure to features that are closely spaced within a structure. Air pores with spacings of 213 nm become larger than designed, as the PMMA is exposed from the direct write of the circle and then again from the electron scattering when nearest neighbors are written. During etching, the ions can etch in both dimensions, although one chooses the gases to be as anisotropic as possible (mostly etching in the vertical direction), the features in the resist can be etched to a larger or smaller diameter depending on the etching conditions. Write field (WF) stitching errors occur as the sample is shifted under the e-beam to write a new WF. Fluctuations in the actual position of the sample, as opposed to the expected position of the sample, result in shifts of the WF in vertical and horizontal directions. This is known as a stitching error. Both the proximity and etching effects produce systematic errors, which modify all air pores within the lattice. While the stitching error is in some sense systematic, as the entire WF is shifted, the resulting discontinuity is random in that the size of the shift in any direction is not predictable and, in fact, will vary from one WF to another (Fig. 6). We discuss ways to minimize these three effects experimentally through the design of the PBG structure, use of alignment marks in the writing process, and through control of external writing conditions; some errors are, however, inevitable. Modeling of these fabrication errors provides insight into the magnitude of each error, which can be tolerated until the device efficiency is compromised.

5. 1. Air pore diameter inconsistencies

As just stated, in the e-beam exposure, developing, and etching stages, the air pores will not be exactly the same diameter as our initial designs. This introduces difficulties if the diameter increases to the point that the lattice no longer has a photonic band gap for the wavelengths of interest for our WDDM. Unlike the field stitching error, variation in air pore diameters can be minimized by proximity correction or initial design modification. Experimentally, we used a

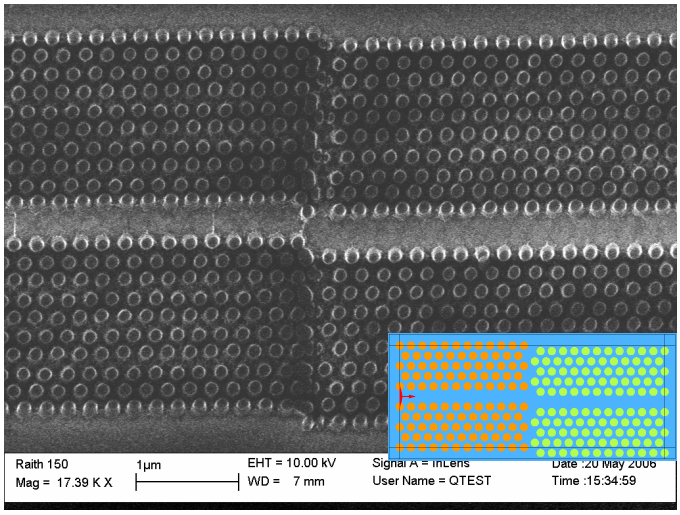

Fig. 6. An SEM image of a photonic crystal waveguide with a defect caused by the field stitching error written by the Raith 150 e-beam system. The embedded figure is the model of a simple waveguide written in different WFs. The color (orange and green) represents different WF.

design radius of 60 nm for the photonic lattice, and 115 nm and 130 nm respectively for the 514.5 nm and 496.5 nm defect cavities. To predict the losses one would encounter due to air pore variation, a simple triangular photonic crystal, 24 x 11 lattice of air pores with a waveguide at the sixth row is created. When we simulate these errors by changing the entire lattice of air pores' diameters arbitrarily from -10 nm to 10 nm from the expected diameters, we find that the waveguide output showed no significant loss (less than 2%). Such a result is expected as the photonic band gap exists for a range of air pore diameters (see Fig. 1), and as

#71934 - $15.00 USD Received 13 June 2006; revised 7 August 2006; accepted 8 August 2006

long as the designed structure falls within these parameters the PBG structure should operate as designed. Thus if we are able to fabricate air pores to within ±10 nm of their expected values, our device should still have a high efficiency output.

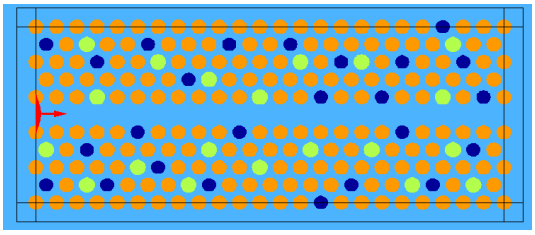

Fig. 7. PBG lattice with randomly distributed air pore imperfections, blue are 140 nm diameter, orange are the expected 150 nm, and green pores are 160 nm in diameter.

On occasion, during the e-beam exposure and subsequent fabrication steps, individual air pores may not be exactly the same size. The random variation in air pore size is measured in our initial fabrication runs. A linescan of an SEM across 11 air pores in the developed PMMA lattice produced an experimental air pore radius variability 74.8 ± 1.4 nm. Dusts, chip imperfections, resist impurities, and chemical processing can all contribute to such variations. We model such inconsistencies by randomly varying the size of air pores within the PBG lattice from 140 nm to 160 nm around a single waveguide (see Fig. 7). No significant loss is found upon launching a beam down this modified waveguide. Again, this is not surprising. In fact, until an air pore within the body of the lattice reaches the diameter of the defect cavities (range of 230-260 nm), it will not trap a significant portion of the light.

Another proximity error in e-beam lithography occurs along the edge of the waveguide structures. Here the last row of air pores experiences less proximity effect due to fact that one row of air pores is missing, which forms the waveguide, thus, the row of air pores along the edge of the waveguide tend to be somewhat smaller. When the transmission of the a linear waveguide is modeled as the row of air pores along the edge of the waveguide is varied from 100 to 180 nm in diameter, we find that there is no effect on transmission for air pores that are smaller than the 150 nm range (recall the goal is 150 nm diameter pores), but that when the air pores reach 160 nm and greater, the transmission drops significantly with a transmission of 50% at 160 nm and then below 10% at 170 and above (modeled with the 514.5 nm wavelength input). This can be attributed to the fact that as the pore size increases the waveguide width decreases until it reaches a point that the 514.5 nm light can no longer propagate through the structure – there are no propagating modes allowed. One can see this effect in Fig. 4(a) where the 514.5 nm light is unable to propagate down the narrower waveguide structure after its coupling cavity.

In Fig. 7, the initial fabrication runs resulted in air pores that were 75 ± 5 nm in radius through the e-beam exposure and development stages, which is well within the predicted range for a PBG to exist for our wavelengths, so the etching step will be the last hurtle to overcome in that regard. However, the resonant coupling cavities also changed size during e-beam exposure and present another question about the WDDM efficiency.

#71934 - $15.00 USD Received 13 June 2006; revised 7 August 2006; accepted 8 August 2006

(a) (b)

Fig. 8. Defect Fabrication error. (a) model for 496.5nm line with defect fabrication error. (b) SEM image of overlapped air pore and cavity for 496.5nm line

The resonant coupling cavities also tend to expand during the fabrication process; this is another factor which could contribute to transmission losses in the WDDM. In fact, Fig. 8(b) shows how the 496.5 wavelength defect cavity increases in diameter by ~10 nm during e-beam lithography due to the proximity effect. The 514.5 nm wavelength defect cavity experiences similar increase. This is further complicated by the fact that the designed coupling cavity is only 13 nm from the nearest PBG lattice air pores in the 514.5 nm coupler, and a mere 3 nm from nearest air pores in the 496.5 nm coupler. Such a small design separation translates into a coupler that is actually connected to its nearest air pore neighbors as seen in Fig. 8, creating a "daisy" structure. We simulate this effect, as shown in Fig. 8 (a) for each coupling cavity in the WDDM structure. For Channel 1 (514.5 nm input), the usual output efficiency is 86.6%, but with the more realistic output coupling cavity configuration we find the output would be decreased to74.3% with the Channel 2 output increasing to 9.5% from 4.1%. For Channel 2 (496.5 nm input), the connected coupler decreases the efficiency from 86.7% to 67.9%. Clearly this proximity effect-related difficulty will have the greatest effect on the output efficiency of the WDDM device. To avoid this, further changes in the initial design could be made including using a smaller design radius for the coupling defect and the nearest neighbor air pores, along with lowering the dosage of nearest neighbor air pores. Such design considerations may reduce or eliminate this proximity effect problem.

5.2. Stitching errors between write fields

In the e-beam lithography fabrication process, a typical WF size is 100μm by 100μm during exposure. As seen in Fig. 4, our two-channel WDDM can fit easily within one WF. However, an actual device must couple laser light into the WDDM device area, and then guide light out of the channels so that one can acquire the signals at the edge of the chip. Thus many WFs are necessary to write the PBG lattice for guiding the light into and away from the WDDM. An example of such stitching errors is found in the SEM micrograph in Fig. 6. This SEM comes from an initial run as we characterized the fabrication process. The stitching error in this micrograph is a "worst" case scenario, as no alignment markers were used in the different WFs to reset the e-beam origin. The Raith 150 e-beam lithography system has specifications for stitching errors of 60 nm for three standard deviations, which is an average as defined by a Gaussian distribution of measured stitching error from a multi-exposure test pattern. In fact, our particular system had a 24.4 nm width for three standard deviations when it was installed. This specification is based on the use of alignment markers in each WF. For our device structure, it will be possible to use alignment markers and therefore minimize the stitching error, since the PBG lattice only needs to contain a dozen rows on each side of the waveguide for adequate confinement of the beam. Thus the error denoted in Fig. 6 provides a measure of the largest offset one might expect in the fabrication process. Note that we see ~155 nm shift in the vertical direction (across the waveguide) and about 90 nm shift of the WF along the

#71934 - $15.00 USD Received 13 June 2006; revised 7 August 2006; accepted 8 August 2006

waveguide, or horizontally. We use these results to model the affect of such stitching error on the WDDM operation.

Our aim is to model the transmission loss due to the unwanted errors from vertical or horizontal shifts of the chip, which occur during feature writing. To predict the losses one would encounter due to such imperfections introduced by fabrication, the same 24 x 11 lattice of air pores with a waveguide at the sixth row is used as above. Then, we divide the waveguide into two parts [Orange and green in Fig. 6 (inset of figure)], as if it is written in different consecutive WF's.

First, the transmission of the waveguide is studied as a horizontal shift or gap between the waveguides is introduced. The horizontal gap is incremented by 10 nm up to a full lattice constant, and the data are recorded by measuring the average steady state intensity at the end of the waveguide. The normalized output intensity (ratio of output intensity, I, to input intensity, Io) at the end of the waveguide (blue) is recorded for each gap (Fig. 9). We find that the transmission efficiency drops below 50% when the horizontal gap increases to between 120 nm and 155 nm with 30% minimum transmission when the gap is 147 nm. This would correspond to the actual waveguide width if we measure the defect width from edge to edge of the separated waveguide air pores. Interestingly, as the gap increases further the transmission started begins to increase reaching ≈80% when the gap is above 176 nm. This increased transmission occurs because as the gap increases, the defect becomes a zigzag waveguide and the light propagating through the defect undergoes multiple reflections. These reflections allow the guided modes to couple back into and continue down the second portion of the waveguide, and the transmission efficiency maintains this efficiency for further gap increases. Following the same procedure, a vertical shift is simulated in step-wise fashion, and the resulting transmission is monitored. When the vertical shift between the waveguides is between 230nm and 340 nm, the waveguide transmission falls below 50% with a minimum transmission of 21% at 270 nm vertical shifts.

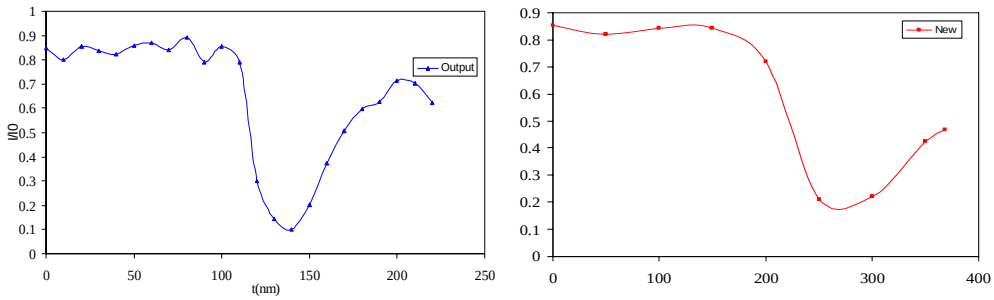

(a) (b)

Fig. 9. Transmission intensity as a function of a) horizontal stitching error and b) vertical stitching error .

The experimental stitching error recorded in Fig. 6 (155 nm vertically and 97 nm horizontally) is within the modeled range for high transmission for the waveguide and output coupling channels. With the additional use of alignment markers during e-beam exposure, such errors should be minimized even further.

6. Conclusion

In this work, we have successfully designed and modeled a high efficiency wavelength demultiplexer for two different argon laser lines, 514.5 nm and 496.5 nm, using a triangular photonic lattice in a planar waveguide structure. By implementing a PBG semi reflector with a high Q factor-coupling cavity augmented by specific waveguide widths, we have determined

#71934 - $15.00 USD Received 13 June 2006; revised 7 August 2006; accepted 8 August 2006

the efficiency of the transmission for each single line wavelength within the demultiplexer to be 86.6% (for 514.5 nm input source) for Output Channel 1 and 86.7% (for 496.5 nm input source) for Output Channel 2. Further, we have considered the challenges inherent in actual fabrication processes used to produce such a device structure. We have predicted the transmission losses due to a vertical and a horizontal shift due to the field stitching error, and have modeled the effect of air pore diameter variation including that of the coupling cavity. In order for the modeling to be realistic, our initial estimates of the magnitude of these errors came from early fabrication runs. Through this modeling, we show that one can expect to be able to fabricate an operational device with reasonable tolerance to such errors. Our next generation of the photonic crystal based wavelength demultiplexer will be based on these new findings.

Acknowledgment

We would like to acknowledge the support of Miami University's, Office for the Advancement of Research and Scholarship for the EMPLab and EMPhotonics Computer. We wish to thank NSF-MRI for their support of the Raith 150 E-beam lithography system through Grant #0216374.

#71934 - $15.00 USD Received 13 June 2006; revised 7 August 2006; accepted 8 August 2006